Carbon 173 (2021) 705–714

Contents lists available at ScienceDirect

Carbon

journal homepage: www.elsevier.com/locate/carbon

Research Article

Evaporation-driven 3D CNT scaffolding for composite reinforcement

A. Nissenbaum[*,1], I. Greenfeld [1], H.D. Wagner[**]

Department of Materials and Interfaces, Weizmann Institute of Science, Rehovot, 76100, Israel

ARTICLE INFO

Article history:
Received 13 August 2020
Received in revised form
26 October 2020
Accepted 12 November 2020

Keywords:
CNT
Scaffold
Evaporation-deposition
Composite

ABSTRACT

The reinforcement of composites by carbon-nanotubes (CNTs) is typically limited by agglomeration and non-uniform dispersion. Thus, achieving a nanocomposite with high density of reinforcement material is a tough challenge. In this work, rather than mixing CNTs in a matrix, we first construct a dense CNT-network scaffold, and then impregnate it by the matrix to obtain a composite. To that end, we explore an evaporation-driven self-assembly approach to form 3D CNT scaffolds on quartz fibers, which combines high CNT density and nanoscale pore size with a straightforward, efficient process. The scaffold is thicker than the fiber by more than an order of magnitude, with a typical pore size of 70 nm and porosity of 60%. The strength of a scaffold-reinforced composite is evaluated by a fragmentation test. μCT 3D-reconstruction of the fragmented scaffold reveals that the matrix-impregnated scaffold creates a multiscale structure that under load behaves much like a fibrous composite. The fragmentation results are analyzed by a mechanical model, demonstrating a scaffold-composite strength of ~200 MPa. The improved strength and relatively high CNT volume fraction (~20%), along with the capability of tuning the scaffold thickness and density, make the proposed structure a promising prospect for composite reinforcement, as well as for diverse nanoscale applications.

1. Introduction

Recently, carbon nanomaterials have been of growing interest in the assembly of 3D CNT scaffold structures, especially in the fast growing tissue-engineering field [1]. 3D scaffolds demand considerable mechanical stability and strength, and consequently CNTs emerged as a potential candidate for such structures. However, as opposed to 2D structures such as thin films, templating 3D CNT scaffolds prove to be a challenging task. There are two types of CNT scaffolds: those comprised entirely of CNTs without inclusion of polymers, and polymeric scaffolds that incorporate CNTs as a structural additive. While the former has the advantage of improved mechanical properties, it suffers from limited fabrication methods and process control. The latter, on the other hand, enables easier and controllable fabrication, but suffers from low volume fraction of CNTs (typically <5%wt) because of agglomeration.

The main methods to produce 3D CNT scaffolds are freeze casting, electrospinning and gel-formation. Freeze casting involves an anisotropic scaffold growth, induced by solidification of a CNT suspension. While freeze casting enables more control over the CNT volume fraction, orientation and scaffold porosity, it involves complex templating processes that reduce the control over its microstructure [2]. 3D CNT scaffolds can also be made by electrospinning [3], where a small volume fraction of CNTs is incorporated in a matrix material. Although electrospinning scaffolds usually produce aligned CNT microstructures, the process is dependent on many parameters and the low volume fraction of CNTs degrades the potential mechanical properties.

To resolve some of these issues, a new approach is proposed here for the preparation of 3D CNT scaffolds by surfactant-assisted *evaporation-driven self-assembly (EDSA).* In this approach, the scaffold is constructed by self-assembly of CNTs on the surface of a quartz fiber, driven by the evaporative flow of a CNT suspension. The process is straightforward, resulting in a relatively thick porous scaffold (~10^2 μm in diameter) coating the fiber. The scaffold dimensions and microstructure can be controlled by adjusting the CNT type and the solution concentration. In previous EDSA research, the focus was on the nanostructured assembly, morphology and nanoparticles type involved in the deposition process [4–8]. Since these previous experiments were conducted on flat surfaces, the thickness of the resulting assembly was limited to the nanoscale [9,10]. The current study is, to the best knowledge

* Corresponding author.
** Corresponding author.
E-mail addresses: asaf.nissenbaum@weizmann.ac.il (A. Nissenbaum), green_is@netvision.net.il (I. Greenfeld), Daniel.wagner@weizmann.ac.il (H.D. Wagner).
[1] These authors contributed equally to this work.

https://doi.org/10.1016/j.carbon.2020.11.041
0008-6223/

of the authors, the first attempt to construct thick 3D-scaffolds using the EDSA method.

In the current study, we build a nanocomposite by impregnating an EDSA-prepared scaffold by a matrix, so as to obtain high CNT volume fraction and uniformity, otherwise not achievable by conventional mixing of CNTs in matrix. The formation of the scaffolds is carried out by immersing quartz microfibers in a water/SDS-based CNT suspension, with evaporation accelerated by heating. Theoretical analysis of the evaporation-driven deposition shows the effect of the governing process parameters, and clarifies the advantage of fiber deposition over deposition on flat surfaces. The properties of the CNT network, including pore size and porosity, are analyzed. The scaffolds are impregnated by and embedded in an epoxy matrix, and are thereafter subjected to a fragmentation test to determine their strength. The composite microstructure during and after fragmentation is analyzed by means of light and electron microscopy, as well as μCT for 3D reconstruction of the composite internal structure. This is followed by a detailed mechanical analysis of the composite structural strength.

2. Experimental

2.1. CNTs dispersion

The CNTs used throughout the experiments are multi-walled carbon-nanotubes (MWCNT, CVD-grown, >95% purity) acquired from Nanolab. The surfactant in use is Sodium Dodecyl Sulphate (SDS, >98.5% GC) acquired from Sigma-Aldrich. In a typical procedure, MWCNTs (10 mg) were added to DI water (100 mL). The solution was sonicated for 20 min. SDS (0.5 g) was then added, and the solution was further sonicated for 20 min. This two-step sonication provides better dispersion, as the first cycle separates out the bundled CNTs and creates more space for surfactant penetration [11]. The surfactant concentration corresponds to 17 mM, well above the critical micelle concentration CMC (7–10 mM [12]), enabling the formation of surfactant nanostructures. To sort the CNTs by their physical structure (size and mass), the solution was centrifuged (RC5C Plus, Sorval) at 4000 rpm for 30 min, yielding homogenous stable CNT dispersion. As centrifugation decreases the initial concentration, UV–Vis (300Bio, Cary) was used to calibrate the solution concentration, applying the solution absorbance to detect the centrifuged solution concentration (Supplementary material S1).

2.2. Self-assembly deposition of CNTs on quartz fibers

Quartz fibers (Quartzel QS-13, ~9 μm diameter, Saint-Gobain) were used as substrate. The fibers were submerged in acetone and rinsed to remove the commercial sizing (to avoid unknown interactions) and were dried afterwards [13]. Bundles of quartz fibers were separated from a spool and immersed and mildly sonicated in ethanol to remove dust and contaminants. Single fibers were manually detached from the bundle, and 0.25 g iron weights were glued to their ends. The fibers were then vertically immersed in a round glass flask containing the CNT suspension. The flask was placed in an oven (Carbolite) and heated to 80 °C to expedite the EDSA process, which lasted until complete evaporation of the liquid. Then the fibers were immersed in water for the removal of excess surfactant. See also Supplementary material S2.

2.3. Characterization of CNT 3D scaffolds

2.3.1. Thermal gravimetrical analysis (TGA)

To evaluate the CNT and SDS fractions within the coating of the quartz fiber, coated quartz fibers were heated by TGA (SDT Q600, TA instruments) from 20 °C to 900 °C at a heating rate of 100 °C/min under a nitrogen environment.

2.3.2. Scanning electron microscopy (SEM)

Images of the 3D scaffolds and the fragmentation specimens were obtained using SUPRA55 scanning electron microscope (Zeiss), at a working distance of 5 mm and beam energy of 5 kV. Prior to scanning, all the samples were sputter-coated with Pd/Ag nanoparticles (S-150, Edwards).

2.3.3. Volume fraction of CNTs in a scaffold

The volume fraction of CNTs within a scaffold (V_c), was calculated using the weight fraction of CNTs extracted from the TGA analysis and the dimensions of the scaffold obtained by SEM measurements. The fraction is given by the ratio of the CNTs volume within the scaffold (v_c) and the volume of the entire scaffold (v_T):

$$V_c = \frac{v_c}{v_T} = \frac{m_c/\rho_c}{\frac{\pi}{4}\left(D_t^2 - D_f^2\right)L} \tag{1}$$

where m_c is the weight of CNTs calculated by TGA analysis, ρ_c is the CNTs density (1.7 g cm^{-3}), D_t and D_f are the scaffold and fiber diameters, respectively, and L is the length of the TGA sample. Similarly, the volume of the SDS surfactant (v_s) and its volume fraction (V_s) are calculated using the surfactant weight and density (1.01 g cm^{-3}). The calculation takes into account the volume of the voids that are contained in the scaffold, which have no mass. The porosity of the scaffold is calculated by:

$$\%porosity = 1 - \frac{v_c + v_s}{v_T} \tag{2}$$

2.3.4. 3D scaffold composite fragmentation test

Single-fiber fragmentation test specimens were prepared by placing a CNT-coated quartz fiber in a dog-bone shaped mold containing Epon-828 (polymerG) epoxy matrix. The sample was cured for 6 h at 100 °C. SEM images of cross sections through the samples showed full impregnation, without bubbles or voids. Mechanical tests were then carried out with a Minimat2000 mini-tensile tester at a displacement rate of 0.1 mm min^{-1}. The stress distribution in the epoxy was monitored by a polarizing optical microscope (POM, Nikon) and recorded by a video camera.

2.3.5. 3D scaffold composite micro-computed tomography (μCT)

To analyze the cracks that are formed in such opaque, hierarchical structure, fragmented samples were scanned by μCT. Fractured dog-bone samples were vertically mounted on a holder and scanned by microXCT-400 (XRadia, Pleasanton, CA, USA). High resolution scans were obtained at 40 kV and 200 μA. The raw imagery data were reconstructed to form 3D images of the samples, using the XRadia software with a filtered back projection algorithm. Slice visualization was carried out with Avizo software (VSG).

3. Results and discussion

3.1. CNT scaffolding using evaporation-driven deposition

Surfactant-assisted EDSA is a soft-template method, in which the ordered formation of the surfactant molecules in the solution is used to co-assemble nanoparticles in an ordered fashion. Although, in principle, surfactant-assisted EDSA can be performed with varying surfactant concentrations, either below the CMC or above

it, surfactants will only form ordered nanostructures when their concentration in the solution exceeds the CMC [14]. Moreover, since the surface tension of the solution is an important parameter, high excess of surfactant is required to maintain a constant surface tension throughout the EDSA process. Here, the CNTs scaffold is constructed by templates of surfactant molecules that surround the CNTs, which are translated toward the fiber surface by evaporation-induced flow. A schematic of the EDSA process is shown in Fig. 1A, and more details on the process are provided in Supplementary material S2.

Under evaporation, the SDS surfactant does not evaporate but solidifies, and has been shown to crystallize into nano- or micro-scale platelets that are attached together to form a template of porous structure [15]. Here, the inclusion of CNTs results in a similar structure, where the CNTs are fused within the SDS particles (Supplementary S3). The porous structure of the scaffold, having an average pore diameter of 76 nm, is similar to other SDS-CNT systems [15]. The similarity, even though different nanoparticles are being used, demonstrates the direct effect of the surfactant type on the morphology. Scaffold pores are commonly divided into macro, micro and nano pores, where each class contributes to different functions. Of relevance to our technique, pores smaller than 100 nm were found to be important in the formation of biological extracellular matrix, among other functions [16]. Although the pore diameter histogram (Fig. 1F) displays a slightly left skewed distribution that spans up to ~300 nm, the 95% confidence level is set between 70 nm and 80 nm in diameter (Supplementary material S3). This pore size is significantly smaller than the size achievable by comparable methods such as freeze casting and electrospinning.

When surfactant soft template is used, it is sometimes possible to remove the surfactant template either by calcination (that is, burning the organic surfactant at ~500 °C) or by dissolution in a solvent. In our study, calcination caused the entire scaffold to collapse and therefore was not applicable. However, immersion of the scaffolds in water did remove most of the SDS, leaving the volume fraction of SDS at an average of 18% (Fig. 1E). The percent porosity of the scaffold is ~60% (Fig. 1E). We plan to improve the process in order to remove trapped SDS particles, which can lead to an optimal porosity of about 80%, comparable to other high-porosity scaffolds [17]. The removal of surfactant particles is expected to contribute to better mechanical properties of the composite due to more intimate contact between the CNTs and the epoxy matrix.

The nanostructure of the CNTs in the scaffold appears to be random with no preferred orientation (Fig. 1C). This is likely because the individual CNTs are longer than the SDS platelets (Fig. S2). Consequently, a single nanotube is too large to be contained in a pore, and the CNTs are expected to cause a disruption in the SDS co-assembly and packing. Furthermore, the high concentration of SDS gives rise to surfactant aggregation, which induce disorder in the scaffold nanostructures [18]. Hence, we did not observe a formation of CNT aggregate regions or inhomogeneous deposition, as also evidenced by the increase of the mechanical properties, discussed later.

By contrast to the nanostructure, the microstructure is characterized by aligned grooves oriented along the fiber axis (Fig. 1B). From the perspective of the SDS-CNT system, Richard et al. showed that when excess SDS is used, the SDS chain adheres to the CNT in the form of half a cylinder [12]. This formation can possibly encourage directionality when a significant amount of CNTs are brought together. From the EDSA physical mechanism perspective, we propose in the next section that these grooves are the result of a strong dependency of the scaffold deposition on the local roughness of the fiber and previously deposited area.

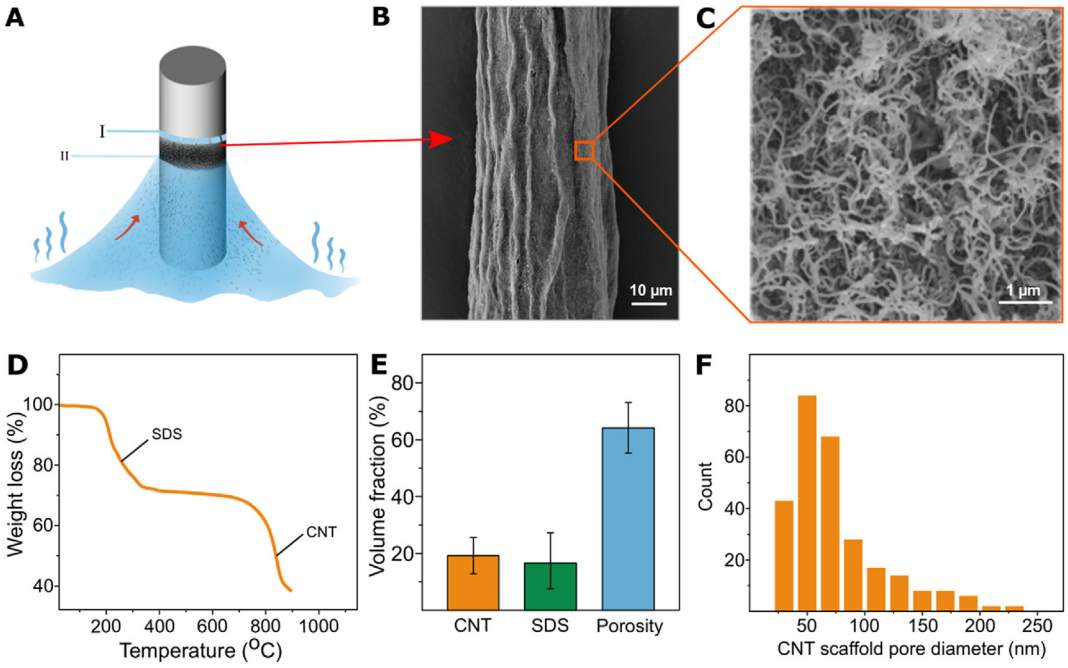

Fig. 1. Description of evaporation-driven self-assembly (EDSA). A - Schematic illustration of the EDSA process: the fiber (gray cylinder) is immersed in a liquid suspension of CNTs and surfactant in water, forming a curved meniscus. The red arrows designate the flow of CNTs toward the meniscus contact line between the liquid and the quartz fiber surface. In the beginning of the process (I), evaporation drives the flow of CNTs to the meniscus region and the volume of the liquid decreases over time. During evaporation, the CNTs adhere to the fiber surface, and as the meniscus contact line recedes with evaporation (II) the CNTs are left deposited on the fiber surface. **B** – CNT scaffold; at the microscale, CNT ribbons are oriented along the fiber axis. **C** – At the nanoscale, the CNTs are seen to be randomly oriented. **D** - TGA analysis of the CNT scaffold. The TGA sample consists of quartz fiber, CNT and SDS surfactant. Each drop in the graph corresponds to the weight loss of each material type during the heating, as marked. **E** – CNT scaffold – CNT volume fraction, SDS volume fraction and scaffold percent porosity, calculated with Equations (1) and (2). **F** – Histogram of scaffold pores diameter. (A colour version of this figure can be viewed online.)

3.2. Scaling analysis of EDSA scaffolding

The scaffold is remarkably thicker than the fiber, indicating massive CNTs transport toward the meniscus tip as a result of solution flow from the meniscus bulk to the tip. The following scaling analysis relates the flow flux to the evaporation of the solvent, and shows how the pinning of the meniscus contact line to the fiber allows enough dwelling time for substantial deposition of CNTs. The CNT-water solution rises on the fiber due to surface tension, forming a meniscus with the shape of a catenary [19] (red line in Fig. 2A).

The deposited CNTs create a mesh soaked by water, and therefore the contact between the solution and the fiber is mostly water-water rather than water-fiber, resulting in a nearly zero contact angle θ_c. The catenary is a zero curvature surface because there is no pressure difference between the reservoir and the meniscus [19]. Nonetheless, the evaporation rate from the catenary surface, J, rises sharply toward the meniscus tip because the vapor concentration above the tip is much lower than below it. The evaporation rate scales as $J \sim J_0 x^{-\lambda}$, where J_0 is the reservoir evaporation rate and x is the downward distance from the tip [20,21]. The rate diverges close to the tip ($x = 0$), reminiscent of an electrostatic field near a sharp edge. The exponent for a catenary with zero contact angle is $\lambda \cong 0.4$, based on finite element analysis of an equivalent electrostatic field (Supplementary material S4).

Considering a small annular liquid wedge of height x and radial thickness w (Fig. 2A), the ingoing volumetric rate, $\sim vw$ (v is the liquid upward velocity) equals the outgoing rate,$\sim Jx$. As in a catenary $w \sim x^2$ for small x, the velocity scales as $v \sim Jx/w \sim J_0 x^{-(1+\lambda)}$. Thus, the velocity diverges toward the tip at a power of about -1.4, generating a high flux of CNTs toward the tip. A CNT starting its travel at distance x from the tip, will reach the tip within $t \sim \int_x^0 dx/v \sim J_0^{-1} x^{2+\lambda}$. The amount of CNTs swept to the tip during that time is the amount included in the meniscus volume above position x, that is $m \sim \varphi_c \int_0^x w dx \sim \varphi_c x^3$, where φ_c is the CNTs volume fraction in the solution. Thus, the transported mass grows in time as

$$m \sim \varphi_c (J_0 t)^{3/(2+\lambda)} \tag{3}$$

where the exponent is ~1.25. This result is valid for a short duration t (small x), whereas for longer durations the exponent of t increases sharply (~7). These relationships indicate that the mass transfer rate grows exponentially in time, initially at a low exponent and then at a much higher exponent. In other words, for longer times mass entrained from regions far away from the tip, where the meniscus is wide, has sufficient time to reach the tip and deposit its load. This behavior is similar to the well-known coffee stain problem [20,21], but with a distinct difference: whereas in the coffee stain the reservoir is confined and limited to a single drop and the liquid surface is nearly flat, in the case of the meniscus the reservoir is practically infinite and the meniscus radius increases dramatically close to the reservoir surface (~1.5 mm). This explains the high thickness of a scaffold deposited on a fiber, compared to the small amount of particles that can be deposited by a drop on a flat surface.

Due to surface imperfections, the contact line (that is, the meniscus tip) stays pinned to the fiber, but after some time t the reservoir's declining water level pulls the contact line down a distance $p \sim J_0 t$ (the pinning height). Thus, using Equation (3), the amount of material transported to the tip region depends on the pinning height as $m \sim \varphi_c p^{3/(2+\lambda)}$, independent of the reservoir evaporation rate J_0. Finally, the deposited scaffold mass is $m \sim V_c r_t^2 p$, where V_c is the CNT volume fraction in the scaffold (fairly constant for given CNT type and size and surfactant concentration - see section 3.4.4) and r_t is the scaffold external radius. The scaffold mass and the deposited mass are equal, yielding

$$r_t \sim \left(\frac{\varphi_c}{V_c}\right)^{1/2} p^{\frac{1-\lambda}{2(2+\lambda)}} \tag{4}$$

where the exponent of p is only ~0.13, a weak dependence on the pinning height. This result is valid for a small pinning height p (short t), whereas for longer durations the exponent of p increases sharply (~3), and the scaffold radius becomes highly dependent on the pinning height. This strong dependence could explain the scaffold grooves (Fig. 1B), as the pinning height p is sensitive to the fiber local roughness and impurities, which induce local variations in p and consequently local variations in the scaffold radius. The scaffold radius dependence on the CNT volume fraction in the solution is $r_t \sim \varphi_c^{1/2}$, assuming the scaffold radius is much larger than the fiber radius (as is the case in our samples). Other significant parameters that influence the scaffold radius are the fiber radius and contact angle (not presented). The complete model is in agreement with the experimental measurements (Fig. 2B). The model was calculated numerically for fiber radius $r_f = 4.5$ μm,

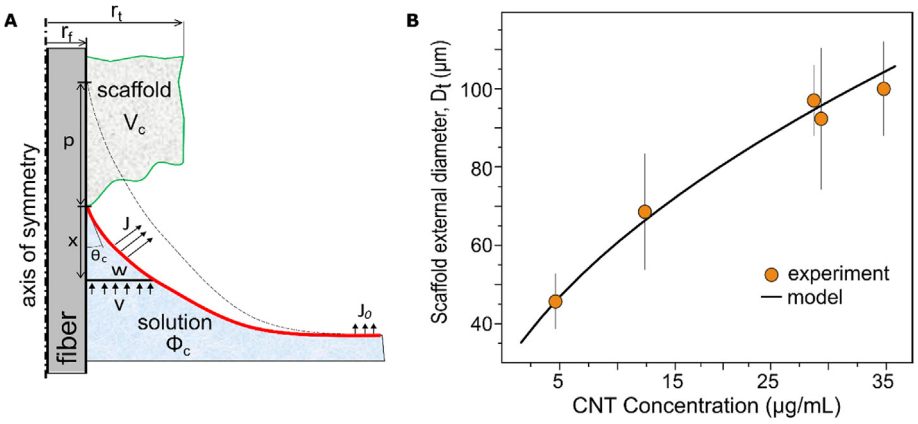

Fig. 2. CNT deposition analysis and measurement. A - A schematic of the air-liquid-solid contact line interface. J_0 is the evaporation flux at the liquid flat surface, whereas J is the varying flux at the meniscus curved surface; v is the flow velocity at position x, φ_c is the CNTs volume fraction in the liquid suspension, and V_c is the CNTs volume fraction in the solid scaffold. **B** - Experimental results and model simulation of the scaffold external diameter, $D_t = 2r_t$, vs. the CNT concentration in the suspension, demonstrating the scaling law $r_t \sim \varphi_c^{1/2}$. (A colour version of this figure can be viewed online.)

contact angle $\theta_c = 0°$, CNT volume fraction in the scaffold $V_c = 0.2$, and pinning height $p = 28$ μm (used as fitting parameter).

3.3. Scaffold fragmentation in a cylindrical reinforced composite

Fragmentation tests were carried out to allow derivation of the cylindrical scaffold composite strength from the fragments average length at saturation. The tested structure included the core fiber, surrounded by a cylindrical CNT scaffold impregnated by the matrix (the *tube*), all embedded in bulk matrix (Fig. 3A). Usually, the specimen for a single-fiber fragmentation test is composed of two physical phases, the fiber and the matrix. Since epoxy is a photo-elastic material, the stress field around a fiber fragment is visible under polarized light microscope. A typical birefringent pattern of a fragmentation test specimen of plain quartz fiber/Epoxy is shown in Fig. 3B and of scaffold-deposited quartz fiber/Epoxy in Fig. 3C. The number of fragments is determined by counting the 'butterfly'-shaped light patterns that represent fragmented sections.

As seen in Fig. 3B and C, the scaffold exhibits many more birefringence patterns compared to a fiber without a scaffold. In contrast to the traditional case of plain single fiber in a transparent matrix, the polarized light microscopy does not provide the ability to distinguish in which component the fragmentation occurred, whether in the fiber, tube or both, as the CNT scaffold obscures the fiber. To overcome this limitation, μCT 3D reconstruction of fragmented samples was carried out (Fig. 3E). The μCT scan shows clear fragments of the CNT coating, whereas the quartz fiber appears intact amidst the imaged region.

This finding is also supported by a considerable fiber pull-out, which suggests extremely weak bonding of the scaffold composite to the fiber surface. The pull-out can be viewed as a smooth hole in the SEM micrograph of the sample cross-section (Fig. 4A). Quartz fiber pullout implies that the quartz fiber undergoes early failure during the tensile loading, and therefore is not likely to contribute much to the strength of the impregnated scaffold. This observation is supported by the poor adsorption seen between the CNT scaffold (prior to impregnation) and the fiber (Supplementary Figure S5.1A-D). Therefore, after impregnation by the matrix, the adhesion between the scaffold and the fiber is mostly due to the matrix-fiber adhesion.

Furthermore, at the scaffold-matrix interface, SEM images display shear cracks of the epoxy matrix around the scaffold, likely emanating from (or due to) high stress concentration at the epoxy matrix/scaffold interphase (Fig. 4B and C). This implies that the dominating interface in terms of shear strength is in fact the interface between the matrix and the epoxy impregnated CNT scaffold. This observation is important to ascertain whether the quartz fiber contributes to the composite and consequently to a correct composite strength calculation. A magnified observation of the fracture surface (Supplementary Figure S5.2) shows that during fracture a small portion of the CNTs pull out from the matrix whereas the majority of CNTs break, indicating that the CNTs are exploited to their full strength.

3.4. Calculation of the CNT scaffold composite strength

3.4.1. Strength derived from critical fragment length

The tensile strength of the epoxy-impregnated CNT scaffold may be calculated from a fragmentation experiment. As seen in Fig. 4A, debonding was observed at the internal (fiber-tube) interface, whereas no debonding took place at the external (tube-matrix) interface. The classic Cottrell-Kelly-Tyson (CKT) model, applied to the tube and fiber assembly embedded in matrix, yields the assembly's critical length [22,23]:

$$\ell_c^{tf} = \frac{\sigma_{tf} D_t}{2\tau_i} \tag{5}$$

where σ_{tf} is the strength of the tube and fiber assembly, D_t is the external diameter of the tube, and τ_i is the interfacial strength of

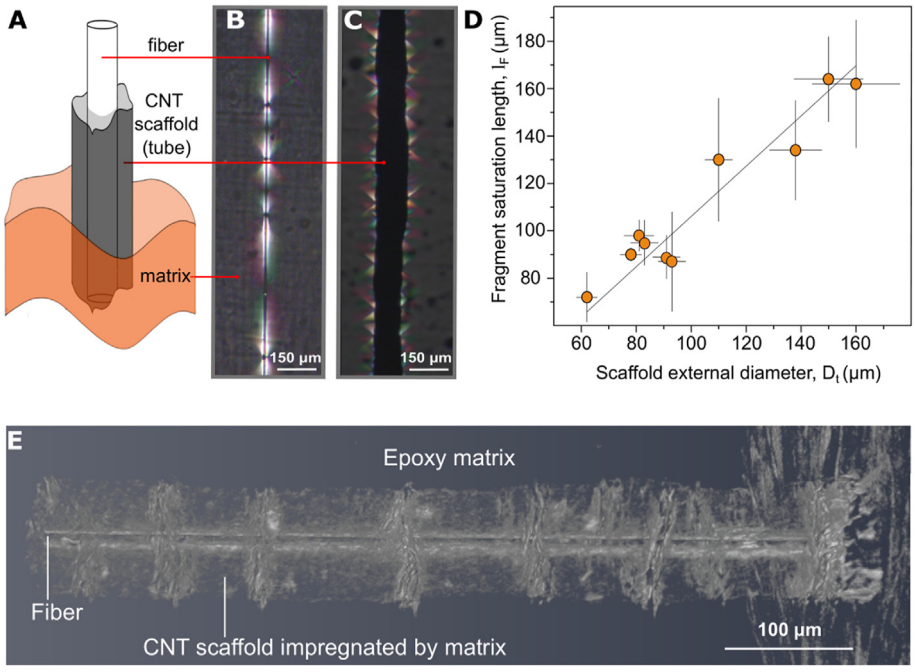

Fig. 3. Fragmentation of a CNT scaffold in a composite under load. A – Illustration of the fragmentation sample – a scaffold-deposited quartz fiber, impregnated by Epoxy and embedded in an Epoxy matrix. **B** – Micrograph of plain quartz fiber/Epoxy composite fragmentation test. **C** – Micrograph of scaffold-deposited quartz fiber/Epoxy composite. **D** - Experimental results of the scaffold fragment saturation length (l_F) vs. the scaffold external diameter (D_t). The slope of the linear fit is 1.06. **E** – 3D reconstruction of fragmentation sample using μCT. (A colour version of this figure can be viewed online.)

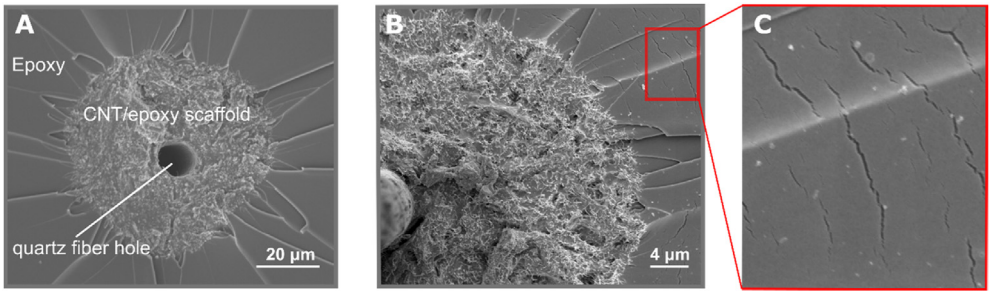

Fig. 4. Fracture surface after fragmentation test. A - SEM micrograph of a fracture surface; each phase is marked in the figure. The hole is the result of quartz fiber pullout during the test. **B** – SEM micrograph of a fracture surface. Shear cracks appear radially at the epoxy-scaffold interphase. **C** – Magnified image of the matrix shear cracks. (A colour version of this figure can be viewed online.)

the tube-matrix (external) interface. The critical length represents the length above which the assembly will break as a result of a maximum stress higher than σ_{tf}, whereas below the critical length the assembly will not break because the maximum stress that builds up in the assembly is lower than σ_{tf}.

The CKT model assumes uniform shear stress along the tube interface, equal to the matrix yield strength, balanced by the tensile stress at the midplane of the tube and fiber assembly. The question arises whether CKT is valid for fragments with such low aspect ratio (length/diameter) as observed here for the scaffold tube (Fig. 3C and D). The concentric shear cracks, observed at the fracture surface (Fig. 4B and C), imply that the matrix interface yielded all along the tube-matrix interface as CKT predicts. This can be inferred from the fact that the fracture occurred at a location where the shear stress was lowest prior to fracture, because this location is in a region of transition from positive to negative stress. Refer, for example, to the FEA (finite element analysis) in Supplementary section S6, where the shear stress (denoted by XY) between the matrix and the tube tends to zero at the midplane. Thus, if the interface at the midplane yielded, all the more so far away from the midplane where the shear stress is higher.

Once fragmentation saturation is reached, the fragments lengths vary uniformly between $\ell_c^{tf}/2$ and ℓ_c^{tf}, on average $3/4\ell_c^{tf}$, as longer fragments will continue breaking whereas shorter ones will not. Thus, the critical length of the tube and fiber assembly is $\ell_c^{tf} = 4/3\ell_F$, where ℓ_F is the experimentally measured average length of the fragments. We can calculate the strength of the tube and fiber assembly by inverting Equation (5):

$$\sigma_{tf} = \frac{2\ell_c^{tf}\tau_i}{D_t} = \frac{8\ell_F\tau_i}{3D_t} \tag{6}$$

To isolate the strength of the tube alone (σ_t) from the tube and fiber assembly, we need to subtract the fiber contribution. The FEA in Supplementary section S6 shows that in a fragment with a critical aspect ratio $\ell_c^{tf}/D_t = 4/3\ell_F/D_t = 1.41$ (as measured in Fig. 3D), the fiber contribution to the tensile load carried by the tube and fiber assembly at the midplane is only 3.7%, assuming no debonding. Furthermore, as the fragmentation test showed that the fiber debonded from its tube interface in most cases, its contribution to the strength of the tube and fiber assembly can be neglected. This observation is supported by the FEA in Supplementary section S6, which shows a divergent shear stress concentration at the sharp corner of the fiber-tube interface, a place for a debonding crack to start propagating. Thus, the fiber is likely to debond at the internal interface, or to break, much earlier than the tube at the external interface. We can therefore neglect the fiber contribution in the calculation of the strength of the tube and fiber assembly, that is $\sigma_{tf} \cong \sigma_t$.

The stress calculated by Equation (6) assumes a solid cylinder (usually a fiber), whereas the scaffold tube is hollow as a result of the cylindrical cavity left by the debonded and pulled-out fiber. Thus, the tube actual strength is higher by the ratio of the cross sectional areas of a solid tube and a hollow tube, that is $r_t^2/(r_t^2 - r_f^2)$. Furthermore, as discussed in the next section, fragments of very small aspect ratio incur a significant tensile stress concentration, associated with nonuniform stress distribution in a cross section. Incorporating these factors in Equation (6), and replacing σ_{tf} by σ_t, the scaffold composite strength is obtained

$$\sigma_t \cong \frac{8\ell_F\tau_i}{3D_t}\frac{r_t^2}{r_t^2 - r_f^2}K \tag{7}$$

$K \equiv \sigma_{max}/\sigma_{nom}$ is the stress concentration factor, where σ_{max} and σ_{nom} are the maximum and nominal (mean) tensile stresses in the tube, respectively, both at the tube midplane cross section where the stress is highest.

The experimental fragmentation results at various scaffold diameters exhibit saturation fragments aspect ratio of $\ell_F/D_t = 1.06 \pm 0.03$ (the slope in Fig. 3D), which is essentially constant over a wide range of scaffold diameters from ~60 μm to ~160 μm. As $\sigma_t \propto \ell_F/D_t$ (Equation (7)), this result implies that the scaffold strength remains fairly constant as well, independent of the tube diameter. This finding further implies that the CNTs density in the scaffold is uniform, regardless of the tube diameter, as significant density variations in scaffolds of different diameters would have resulted in different composite strengths and therefore aspect ratios. The deposition modeling assumption, that the CNT volume fraction in the scaffold is fairly constant for a given CNT type, size, and surfactant concentration, is thus confirmed.

3.4.2. Stress concentration in short fragments

The calculation of the strength of the impregnated scaffold (the tube) using the standard CKT model (Equation (6)) underestimates the actual strength of the scaffold because of stress concentration. The reason for this is that in low-aspect fragments, such as in our scaffold's fragmentation tests, the tensile stress in the tube, induced by the shear stress at the tube-matrix interface, does not propagate efficiently toward the scaffold core. In plain words, the tube is too thick and too short for the stress to spread uniformly in a tube cross section. Consequently, the tensile stress at the fragment midplane, where the tensile stress is highest, is not uniformly distributed. This results in a stress concentration near the fragment outer boundary, causing the scaffold to fracture at a lower load than predicted by the CKT model, exhibiting a lower strength. This stress concentration is expressed by the factor K incorporated in Equation (7); the ensuing strength represents the impregnated scaffold composite strength

were it loaded directly by tension applied on a standalone tube, rather than via shear stresses when embedded in a matrix.

The stress concentration effect is explained and modeled using finite element analysis (FEA), summarized in Fig. 5. The CKT model and other similar models assume uniform tensile stress distribution in each cross-section of a fiber, an assumption that is true for common fibers such as carbon and glass fibers, whose critical aspect ratio is typically between 25 and 100. In such fibers, the typical non-uniform stress distribution close to the fiber ends (the edge effect) vanishes toward the fiber midplane where the stress is highest. This means that the fiber's material strength is exploited to its optimum under an ultimate load. By contrast, in short fragments such as in our impregnated scaffold, because the tube is short and thick, this edge effect does not diminish appreciable toward the fiber midplane. The result is a maximum stress at the midplane that is significantly higher than the mean stress at that cross-section. In other words, in short fragments the edge effect is significant, whereas in long fragments the edge effect gradually diminishes sufficiently far from the edge (the well-known Saint Venant's principle in solid mechanics).

This is clearly seen in the stress distribution in the midplane of a scaffold fragment with a critical aspect of 1.41 (Fig. 5C), compared to a theoretical fragment with a larger aspect of 5 (Fig. 5D). Midplane stress distribution for fragments of several aspects is shown in Fig. 5B (inset). Defining the stress concentration K as the ratio between the midplane maximum stress and mean (average) stress, we can depict K as a function of the fragment aspect ratio (Fig. 5B). The stress concentration is seen to rise sharply for fragments with aspect below 3, with a value of $K \cong 1.33$ for a critical fragment. Thus, the strength of the fragment is dominated by the maximum stress rather than the mean stress, and is therefore higher than predicted by the CKT model.

Using this value of stress concentration we return to the calculation of the tube strength according to Equation (7). As the tube-matrix interface is mostly an epoxy-epoxy interface, the shear strength of the matrix, τ_i, has about the same magnitude as the tensile strength of epoxy, σ_m, thus $\tau_i \cong \sigma_m \cong 50 - 60$ MPa. Inserting these values into Equation (7), the resulting estimate for the

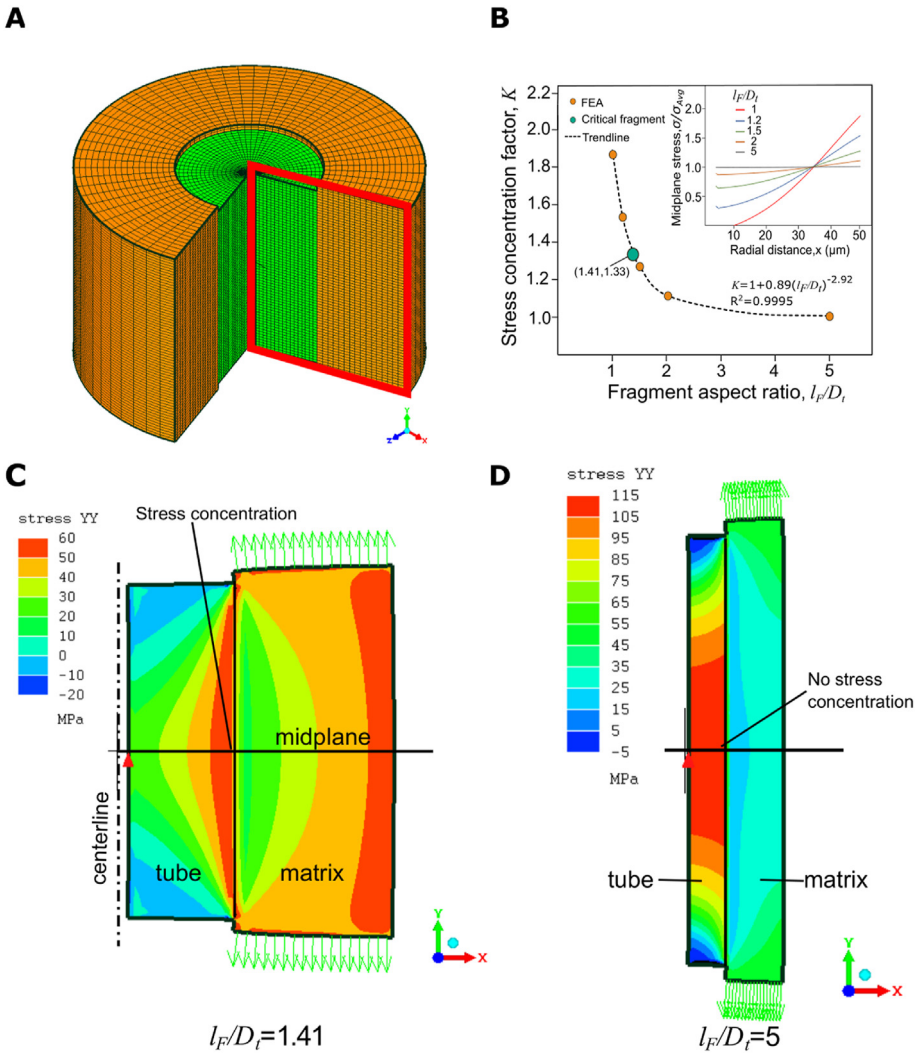

Fig. 5. ***Assessment of stress concentration factor in impregnated tubular scaffold fragment.*** **A** – Axisymmetric model for finite element analysis (FEA), with y-axis as the centerline and x-axis as the radial dimension. The red frame indicates the region of the stress maps presented in C and D. **B** – Tensile stress concentration factor vs. fragment aspect ratio. The critical fragment aspect is indicated by the green dot. Inset: Midplane stress distribution, normalized by the mean stress, for several aspect values. **C** – Tensile stress distribution in a fragment of critical aspect, $\ell_F/D_t = 1.41$. **B** – Tensile stress distribution in a long fragment, $\ell_F/D_t = 5$. The tube internal diameter is $D_f = 9$ μm and its external diameter is $D_t = 50$ μm. The load is a uniform tensile stress of 50 MPa on the upper and lower faces of the matrix (indicated by green arrows). The matrix and tube elastic moduli used in the model are 1 MPa and 5 MPa, respectively. (A colour version of this figure can be viewed online.)

scaffold tube strength σ_t is 191 MPa (using $\sigma_m = 50$ MPa) or 229 MPa (using $\sigma_m = 60$ MPa). Thus the strength of the reinforced tube composite (the impregnated scaffold), estimated from the fragmentation test, is about fourfold the matrix strength.

3.4.3. Strength derived by mixture rule

We now validate the previous estimation of the value of σ_t, which used the critical length measured in fragmentation tests, by means of the following mixing rule

$$\sigma_t = \eta_l \eta_o V_c \sigma_c + V_s \sigma_s + V_m \sigma_m \tag{8}$$

based on contributions from (left to right) the CNTs, surfactant and matrix, using their respective volume fraction V and strength σ. The CNTs contribution is slightly degraded in view of their finite (though long) length, and by their arbitrary spatial orientation, expressed by the η_l and η_o factors, respectively. For arbitrarily oriented fillers in 3D, as seen in the CNT scaffold in Fig. 1C, the orientation factor is [22] $\eta_o = 1/5$. The length factor is given by $\eta_l = (1 - \ell_c^{CNT}/2\ell^{CNT})$, when the CNT length ℓ^{CNT} is longer than its critical length $\ell_c^{CNT} = \sigma_c D_{CNT}/2\tau_i$ [23]. Thus, equation (8) reduces to

$$\sigma_t = \frac{1}{5}\left(1 - \frac{1}{2}\frac{\ell_c^{CNT}}{\ell^{CNT}}\right) V_c \sigma_c + V_m \sigma_m \tag{9}$$

neglecting the surfactant strength ($\sigma_s \cong 0$). This equation is based on the CKT model, taking into account the fraction of CNTs that break during fracture and those that pull out.

The average strength of CVD-grown multiwall CNTs in Barber et al. [24] was 97.1 GPa, based on the cross-section of the CNT outermost wall only ($t = 0.34$ nm thick) which carries most of the load transferred from the matrix interface (the contribution of the inner layers is negligible because of weak interlayer interactions). Ref. [24] provides data on the same CNT type used here (CVD-grown), not available in previous publications such as Ref. [25], where arc-grown CNTs were measured. In the present work the CNTs average diameter was $D_{CNT} = 30$ nm, therefore the average CNT strength σ_c when considering its entire cross section would be obtained by multiplying 97.1 GPa by $4t/D_{CNT}$, which results in 4.4 GPa. The critical length is 1.3 – 1.1 μmfor $\tau_i \cong 50 -$ 60 MPa, respectively, much shorter than the CNTs length which varies between 5 and 20 μm. The corresponding length factor is on average $\eta_l = 0.95$, meaning that the CNTs contribution to the composite strength is degraded by about 5% because a fraction ℓ_c^{CNT}/ℓ^{CNT} of the CNTs pull out from the matrix rather than break. We use $V_c = 0.2$, $V_s = 0.2$, and $V_m = 0.6$ (same as the porosity), as calculated from weight measurements and the mass densities provided by the manufacturer (Fig. 1E).

Substituting these estimated parameters in Equation (9), the resulting assessment for the scaffold tube strength σ_t is 197 MPa (using $\sigma_m = 50$ MPa) or 204 MPa (using $\sigma_m = 60$ MPa), a bit lower than (but quite close to) the values of 191–229 MPa obtained from the fragmentation experiment described earlier (Equation (7)). The closeness of these results, calculated by two distinct approaches (fragmentation test and mixing rule), attests to the uniformity of the CNT network in the scaffold and to negligible CNT agglomeration. The results reflect a strength improvement of the composite by a factor of 3.4–3.9 with respect to the matrix strength with 20% CNT volume fraction. By comparison, a CNT scaffold, prepared from rolled single-walled CNT forests impregnated by epoxy, exhibited a strength improvement factor of 2.1 with 33% CNT volume fraction [26]. Similarly, a CNT-network, collected during CVD process and impregnated by epoxy, displayed a strength increase factor of 2 with 39% CNT volume fraction [27].

3.4.4. Tuning the scaffold composite strength

The composite strength can be tuned by varying the material and process conditions. Variables that affect the strength are those that change the CNTs volume fraction, V_c, or modify the strength of the material components – CNTs and matrix. We have already shown that V_c is neither affected by the CNTs concentration in the liquid suspension, nor by the reservoir evaporation rate. Instead, V_c can be increased by reducing the surfactant amount, thus freeing space for the CNTs, although this is limited because the surfactant is essential for wetting and prevention of agglomeration. The CNT strength can be improved by using CNTs with a smaller diameter, because, as shown above, their strength is inversely proportional to diameter ($\sigma_c \propto 4t/D_{CNT}$). Finally, V_c can be increased by reducing CNT length, as the entangled network formed by CNTs (Fig. 1C) becomes denser when they are shorter. This effect seems predominant and is therefore modeled in detail in Supplementary material S7, with the results depicted in Fig. 6.

The maximum obtainable composite strength for the material system defined in Fig. 6 is about 500 MPa. At this point, the CNTs are tightly packed in bundles, with volume fraction of 0.8 and length of about 2 μm. By comparison, a tightly packed and aligned CNTs fiber (CNTF) impregnated by epoxy, exhibited a tensile strength of 2.7 GPa, for CVD-grown non-functionalized MWCNTs [28]. Adjusting these values for random CNT orientation (orientation factor $\eta_o = 1/5$), we get a strength value of 540 MPa, close to our prediction. Further experimental substantiation of these predictions is left for future research.

4. Conclusion

This study presents a new self-assembly approach to construct 3D CNT scaffolds using surfactant-assisted *evaporation-driven self-assembly (EDSA)* on the surface of quartz fibers. The resulting solid CNT-scaffold is thick, dense and uniform along the fiber. The diameter of the scaffold is up to two orders of magnitude above the fiber diameter and adjusted experimentally in the range of 60–160 μm. Scaling analysis of the deposition process showed a sharp power-law increase in the evaporative flow, which transports

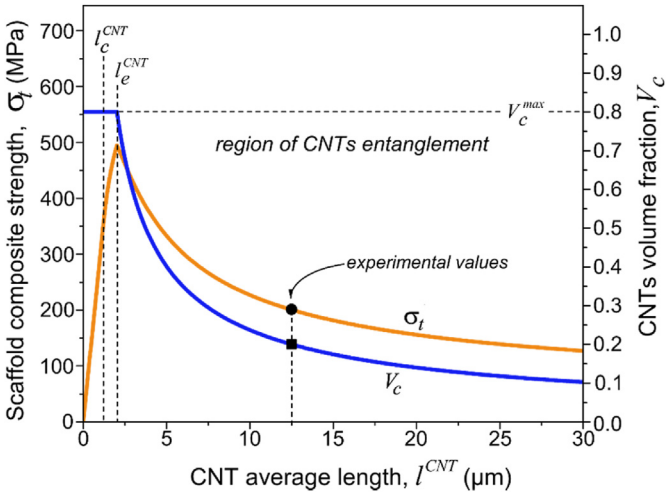

Fig. 6. Theoretical predictions for the scaffold composite strength. The CNT volume fraction and the composite strength are plotted as functions of the CNT average contour length. The experimental values used for model fitting are denoted. l_e is the minimum CNT length to maintain entanglement, and l_c is the CNT critical length. The fitting parameters are: CNT strength $\sigma_c = 4.4$ GPa, matrix strength $\tau_i = \sigma_m = 55$ MPa, CNT diameter $D_{CNT} = 30$ nm multiwall, CNT average length $l_{CNT} = 12.5$ μm, CNT volume fraction $V_c = 0.2$, surfactant volume fraction $V_s = 0.2$. (A colour version of this figure can be viewed online.)

high amount of CNTs to the fiber surface, much higher than on flat surfaces. The properties of the CNT network are analyzed, showing an average pore size in the order of 70 nm, and porosity of 60%. Whereas the vast majority of 3D CNT scaffolds are aimed toward tissue engineering, there is less focus on the application to composites. In this work, to overcome the limitations of mixing CNTs in a matrix, as is usually the case in composites preparation, a dense CNT-network scaffold is first constructed, and then impregnated by a matrix to obtain a composite. We demonstrate the scaffold ability to perform as a reinforcement element in a micro-composite.

The epoxy-impregnated CNT scaffold composite exhibits fiber-like mechanical behavior, whereas the quartz fiber acts as a deposition nucleus rather than a reinforcing component. A fragmentation experiment assisted by μCT analysis reveals short scaffold fragments, with an aspect ratio (scaffold length/diameter) of about 1–2, an order of magnitude smaller compared to fiber-reinforced composites. The aspect ratio remains fairly constant over a wide range of scaffold diameters, attesting to the uniform CNT morphology. The μCT proved to be an adequate tool for the visual differentiation of the hierarchical structural levels within a non-transparent composite.

Mechanical analysis, using both conventional fiber-composite methods and finite element, demonstrates a fourfold increase in the scaffold composite strength with respect to the bulk matrix, achieved with ~20% CNT volume fraction. The analysis was carried out via two complementary approaches, the first based on the critical length measured by the fragmentation test, and the second using a rule of mixture with effective MWCNT strength data from the literature. Both approaches yield similar scaffold strength, even though the former is based on mechanical tests of the scaffold, whereas the latter is based on the CNT strength and dispersion. The finite element analysis revealed high stress concentration near the scaffold's outer boundary, associated with the observed small aspect ratio of the fragments. This is explained by a dominant edge effect at small aspect-ratios, which becomes negligible at the high aspect ratios typical of fiber-reinforced composites. It is also predicted that by reducing CNT length, the composite strength can be further increased up to about 500 MPa.

The nanocomposite concept presented in this study can be used in applications requiring reinforced microscale composites, where microfiber reinforcement is not practical. It could also be used for reinforcement of polymeric coatings protecting delicate micro devices such as optical fibers. Furthermore, the thick cylindrical scaffold achieved by the EDSA method developed here could be used as a structural CNT network in applications requiring nanoscale pore sizes such as in tissue engineering, drug delivery, filters, and probes.

Credit author statement

AN and IG contributed equally to this work. AN prepared the EDSA samples, carried out all experiments and characterization, and wrote the manuscript. IG interpreted the results, carried out the theoretical and simulation analysis, and wrote the manuscript. HDW coordinated the study and edited the manuscript. All authors discussed the results and interpretations and reviewed the manuscript.

Declaration of competing interest

The authors declare that they have no known competing financial interests or personal relationships that could have appeared to influence the work reported in this paper.

Acknowledgements

This research was supported by the generosity of the Harold Perlman family. We also acknowledge support from the G.M.J. Schmidt Minerva Centre of Supramolecular Architectures. H.D.Wagner is the recipient of the Livio Norzi Professorial Chair in Materials Science.

Appendix A. Supplementary data

Supplementary data to this article can be found online at https://doi.org/10.1016/j.carbon.2020.11.041.

References

[1] G. Lalwani, A. Gopalan, M. D'Agati, J. Srinivas Sankaran, S. Judex, Y.-X. Qin, B. Sitharaman, Porous three-dimensional carbon nanotube scaffolds for tissue engineering, J. Biomed. Mater. Res. 103 (2015) 3212–3225, https://doi.org/10.1002/jbm.a.35449.
[2] K.L. Scotti, D.C. Dunand, Freeze casting – A review of processing, microstructure and properties via the open data repository, FreezeCasting.net, Prog. Mater. Sci. 94 (2018) 243–305, https://doi.org/10.1016/j.pmatsci.2018.01.001.
[3] T.D. Stocco, E. Antonioli, M.L. Romagnolli, G.F. Sousa, M. Ferretti, A.O. Lobo, Aligned biomimetic scaffolds based on carbon nanotubes-reinforced polymeric nanofibers for knee meniscus tissue engineering, Mater. Lett. 264 (2020) 127351, https://doi.org/10.1016/J.MATLET.2020.127351.
[4] R.K. Pujala, D. Venkuzhy Sudhakaran, S. Dhara, Evaporation-driven self-assembly in the mixtures of micro and nanoparticles, Bull. Mater. Sci. 43 (2020) 173, https://doi.org/10.1007/s12034-020-02096-5.
[5] H. Machrafi, C. Minetti, V. Miskovic, P.C. Dauby, F. Dubois, C.S. Iorio, Self-assembly of carbon nanotube-based composites by means of evaporation-assisted depositions: importance of drop-by-drop self-assembly on material properties, Mater, Chem. Phys. 218 (2018) 1–9, https://doi.org/10.1016/J.MATCHEMPHYS.2018.06.083.
[6] A.K. Thokchom, Q. Zhou, D.-J. Kim, D. Ha, T. Kim, Characterizing self-assembly and deposition behavior of nanoparticles in inkjet-printed evaporating droplets, Sensor. Actuator. B Chem. 252 (2017) 1063–1070, https://doi.org/10.1016/J.SNB.2017.06.045.
[7] T.A. Shastry, J.-W.T. Seo, J.J. Lopez, H.N. Arnold, J.Z. Kelter, V.K. Sangwan, L.J. Lauhon, T.J. Marks, M.C. Hersam, Large-area, electronically monodisperse, aligned single-walled carbon nanotube thin films fabricated by evaporation-driven self-assembly, Small 9 (2013) 45–51, https://doi.org/10.1002/smll.201201398.
[8] X. Nie, J. Cui, W. Jiang, Ultralong cylindrical micelles precisely located with semiconductor nanorods by solvent evaporation-driven self-assembly, Soft Matter 10 (2014) 8051–8059, https://doi.org/10.1039/C4SM01353K.
[9] K. Livanov, L. Yang, A. Nissenbaum, H.D. Wagner, Interphase tuning for stronger and tougher composites, Sci. Rep. 6 (2016) 26305, https://doi.org/10.1038/srep26305.
[10] L. Xiao, J. Wei, Y. Gao, D. Yang, H. Li, Formation of gradient multiwalled carbon nanotube stripe patterns by using evaporation-induced self-assembly, ACS Appl. Mater. Interfaces 4 (2012) 3811–3817, https://doi.org/10.1021/am300936a.
[11] L. Vaisman, H.D. Wagner, G. Marom, The role of surfactants in dispersion of carbon nanotubes, Adv. Colloid Interface Sci. 128–130 (2006) 37–46, https://doi.org/10.1016/j.cis.2006.11.007.
[12] C. Richard, B. Fabrice, S. Patrick, T.W. Ebbesen, C. Mioskowski, Supramolecular self-assembly of lipid derivatives on carbon nanotubes, Science 300 (2003) 775–779, 80-.
[13] N. Lachman, E. Wiesel, R. Guzman de Villoria, B.L. Wardle, H.D. Wagner, Interfacial load transfer in carbon nanotube/ceramic microfiber hybrid polymer composites, Compos. Sci. Technol. 72 (2012) 1416–1422, https://doi.org/10.1016/j.compscitech.2012.05.015.
[14] O.S. Zueva, O.N. Makshakova, B.Z. Idiyatullin, D.A. Faizullin, N.N. Benevolenskaya, A.O. Borovskaya, E.A. Sharipova, Y.N. Osin, V.V. Salnikov, Y.F. Zuev, Structure and properties of aqueous dispersions of sodium dodecyl sulfate with carbon nanotubes, Russ. Chem. Bull. 65 (2016) 1208–1215, https://doi.org/10.1007/s11172-016-1437-5.
[15] S.D. Kharade, N.B. Pawar, K.V. Khot, P.B. Patil, S.S. Mali, C.K. Hong, P.S. Patil, P.N. Bhosale, Enhanced photoelectrochemical performance of novel p-type MoBiCuSe 4 thin films deposited by a simple surfactant-mediated solution route, RSC Adv. 6 (2016) 24985–24994, https://doi.org/10.1039/c5ra21553f.
[16] I. Bružauskaitė, D. Bironaitė, E. Bagdonas, E. Bernotienė, Scaffolds and cells for tissue regeneration: different scaffold pore sizes—different cell effects, Cytotechnology 68 (2016) 355–369, https://doi.org/10.1007/s10616-015-9895-4.
[17] G. Lalwani, A. Gopalan, J.S. Sankaran, S. Judex, Y. Qin, B. Sitharaman, S. Brook, Porous three-dimensional carbon nanotube scaffolds for tissue engineering. https://doi.org/10.1002/jbm.a.35449.Porous, 2016, 103, 3212-3225.
[18] R.J. Kane Deborah, Micolich Adam, Nanotechnology in Australia, Showcase of Early Career Research, 2011, pp. 228–229.

[19] D. de Gennes, P. G, F. Brochard-Wyart, Quere, Capillarity and Wetting Phenomena - Drops, Bubbles, Pearls, Waves, Springer-Verlag New York, Inc., 2004.
[20] Bakajin Deegan, Huber Dupont, Witten Nagel, Contact line deposits in an evaporating drop, Phys. Rev. E: Stat. Phys., Plasmas, Fluids, Relat. Interdiscip. Top. 62 (2000) 756–765, https://doi.org/10.1103/physreve.62.756.
[21] R.D. Deegan, O. Bakajin, T.F. Dupont, G. Huber, S.R. Nagel, T. a Witten, Capillary flow as the cause of ring stains from dried liquid drops, Lett. to Nat. 389 (1997) 827–829, https://doi.org/10.1038/39827.
[22] M. Piggott, Load Bearing Fiber Composites, Kluwer Academic Publishers, 2002.
[23] I. Greenfeld, H.D. Wagner, Nanocomposite toughness , strength and stiffness : role of filler geometry, Nanocomposites 1 (2015) 3–17, https://doi.org/10.1179/2055033214Y.0000000002.
[24] A.H. Barber, I. Kaplan-Ashiri, S.R. Cohen, R. Tenne, H.D. Wagner, Stochastic strength of nanotubes: an appraisal of available data, Compos. Sci. Technol. 65 (2005) 2380–2384, https://doi.org/10.1016/J.COMPSCITECH.2005.07.021.
[25] M. Yu, Strength and breaking mechanism of multiwalled carbon nanotubes under tensile load, Science 287 (2000) 637–640, https://doi.org/10.1126/science.287.5453.637, 80-.
[26] K. Kobashi, H. Nishino, T. Yamada, D.N. Futaba, M. Yumura, K. Hata, Epoxy composite sheets with a large interfacial area from a high surface area-supplying single-walled carbon nanotube scaffold filler, Carbon N. Y. 49 (2011) 5090–5098, https://doi.org/10.1016/j.carbon.2011.07.028.
[27] A. Mikhalchan, T. Gspann, A. Windle, Aligned carbon nanotube–epoxy composites: the effect of nanotube organization on strength, stiffness, and toughness, J. Mater. Sci. 51 (2016) 10005–10025, https://doi.org/10.1007/s10853-016-0228-6.
[28] X.M. Sui, I. Greenfeld, H. Cohen, X.H. Zhang, Q.W. Li, H.D. Wagner, Multilevel composite using carbon nanotube fibers (CNTF), Compos. Sci. Technol. 137 (2016) 35–43, https://doi.org/10.1016/j.compscitech.2016.10.011.